J Mater Sci (2011) 46:6213–6223
DOI 10.1007/s10853-011-5547-z

ABBASCHIAN FESTSCHRIFT

Influence of solidification variables on the microporosity formation on Al–Cu (4.5 wt%) alloy with axial heat processing

Joo Ro Kim · Reza Abbaschian

Received: 1 December 2010 / Accepted: 6 April 2011 / Published online: 30 April 2011

Abstract The effects of solidification rate, hydrogen concentration, and level of convection on porosity formation in Al–Cu (4.5 wt%) alloys were investigated using Axial Heat Processing (AHP). This processing technique is similar to the conventional directional solidification (DS) technique, except that it utilizes a graphite baffle immersed near the solidification interface to control the shape of the interface and impart an axial temperature gradient. It was found that the samples produced by AHP contained 20–40% less microporosity than similar samples produced by conventional DS. The reduction was also more pronounced with decreasing a cooling rate and increasing an initial hydrogen concentration in the melt. These differences are attributed to the solute accumulation that is due to the confinement of the liquid below the baffle and the concomitant reduction in the convection level near the interface.

List of symbols

DS	Directional solidification by Bridgeman method
AHP	Axial heat processing
G_L	Thermal gradient in liquid (°C/cm)
G_S	Thermal gradient in solid (°C/cm)
V	Solidification rate or pulling rate (cm/s)
P_{H_2}	Hydrogen pressure in liquid Al–Cu alloy
k_S	Thermal conductivity of the solid in the Al–Cu (4.5 wt%) alloy
k_L	Thermal conductivities of the liquid in the Al–Cu (4.5 wt%) alloy
T_m	Liquidus temperature of Al–Cu (4.5 wt%)
ΔP	Pressure drop in mushy zone
P_g	Gas pressure
P_a	Atmospheric pressure
P_σ	Pressure generated by surface tension
P_ρ	Metallostatic head pressure
α	Geometrical portion of interdendritic feeding
g_s	Solid fraction in the mushy zone
β	Contraction factor ($=(\rho_s - \rho_L)/\rho_L$)
ρ_s	Solid density of Al–Cu (4.5 wt%) alloy
ρ_L	Liquid density of Al–Cu (4.5 wt%) alloy
t	Tortuosity of the dendrite
$[H]$	Concentration of hydrogen in the liquid
$[H]_0$	Initial concentration of hydrogen in the liquid before solidification
k_H	Distribution coefficient of hydrogen between solid and liquid
f_H	Activity coefficient
S	Sievert's constant ($cm^3\ atm^{1/2}/100$ g)
C_{Cu}	Copper concentration in Al–Cu alloy
σ	Surface tension
g_l	Liquid fraction in the mushy zone
d_l	Dendrite arm spacing
g_s^*	Critical solid fraction in the mushy zone
g	Magnitude of the acceleration due to gravity
α^*	Thermal expansion coefficient in liquid
d	Diameter of sample
T_s	Temperature at the free surface
Ra_W	Rayleigh number
D_{Cu}	Diffusion coefficient of copper
C_{Cu}^0	Initial copper concentration in Al–Cu alloy
R	Curvature of the dendrite tip

J. R. Kim (✉)
Gemesis Corporation, 7040 Professional Parkway E, Sarasota, FL 34240, USA
e-mail: coolkjr@gmail.com

R. Abbaschian
University of California, Riverside, Dean's Suite, EBU II, Riverside, CA 92521, USA

Introduction

Aluminum alloys have wide applications in the automobile and aerospace industries because of their inherent light weight, resulting in improved performance and fuel efficiency [1]. The alloys also lend themselves easily to casting of complex geometries and cost-effective manufacturing. However, the major drawback for the use of cast alloys relates to casting defects which undermine their performance. One of the most detrimental defects is microporosity which negatively affects mechanical properties, particularly resistance to fatigue [2–6].

Microporosity forms when interdendritic liquid cannot feed the volume shrinkage during solidification that take place near the root of dendrites in the mushy zone [7–10]. Microporosity can also form as gases which evolve because of the solubility difference between liquid and solid. Hydrogen gas evolution is particularly problematic during the casting of aluminum or its alloys, because of the tenfold decrease in solubility upon transformation from liquid to solid [11, 12]. Therefore, even when the liquid contains only a small amount of hydrogen, it can easily become supersaturated between dendrites, resulting in evolution of hydrogen bubbles. When the nucleated gas bubbles fail to escape to the free surface, they become trapped in the growing dendrite colonies or at the grain boundaries as microporosity [13].

Using directional solidification (DS) techniques, thermodynamic and kinetic models as well as computational methods have been used to predict the volume of porosity and its size as a function of processing parameters [1, 14–18]. The processing parameters used in these investigations are the same as those used with the casting variables: thermal gradients in the solid and liquid, solidification rate, initial alloy composition, solute redistribution coefficients, and convection. However, the influence of convection on porosity formation has been particularly difficult to quantify because of the changes in the thermal and solutal gradients as well as the interfacial geometry and melt height as solidification proceeds.

In this research, a solidification technique called Axial Heat Processing (AHP) is used to investigate the effect of solidification variables on the porosity formation Al–Cu (4.5 wt%) alloy, and the results are compared with those of conventional DS. AHP, which recently has been utilized for DS of alloys or single crystal growth [19–21], is similar to the conventional DS technique but a baffle is placed near the solid/liquid (s/l) interface to control the interfacial shape and heat flow. The relationship between s/l interface shape with the baffle and the computational model of heat transfer during solidification has been well established in previous studies [22, 23]. AHP technique has a similarity with the zone melting technique as a small layer of liquid maintained below the baffle travels with the s/l interface and is fed with the original liquid from above the baffle [19]. This confined travelling liquid layer can enhance the solute build up because rejected solutes cannot be mixed effectively with the bulk liquid. Finally, AHP baffle reduces convection as the melt height is significantly reduced. In this study, the influence of AHP technique on the porosity formation mechanism will be compared with that of conventional DS technique.

Experimental procedure

The AHP unit used in study is schematically shown in Fig. 1. The unit consisted of a baffle, (see (1) in Fig. 1), immersed inside the melt and slightly above the dendrite tip in the container (2). Both container and the baffle were made of high-conductivity and high-density graphite coated with zirconium oxide (ZrO_2) mold-wash. A three-zone vertical, tubular furnace (3) was used to provide the required temperature gradients. Six K-type thermocouples were incorporated in the crucible and baffle as shown in the Fig. 1 to monitor axial and radial temperature gradients.

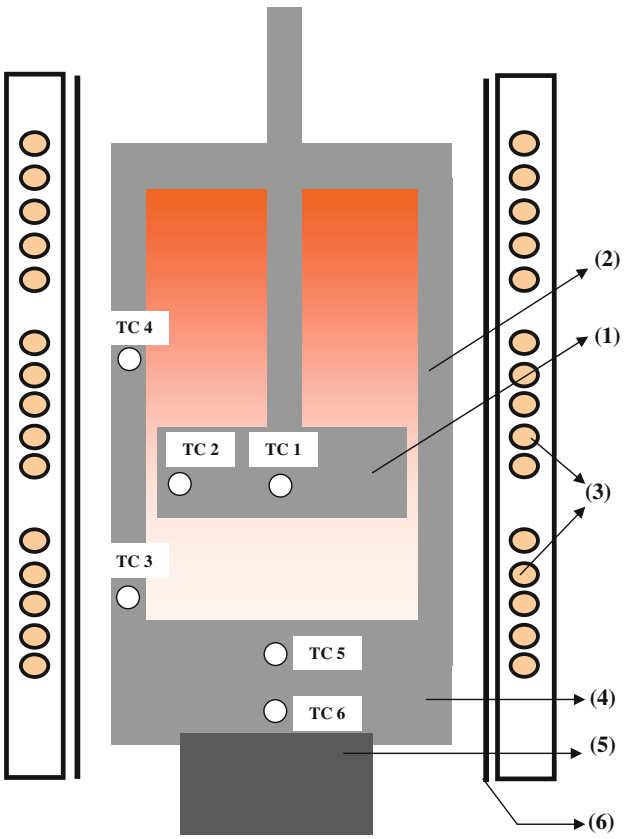

Fig. 1 Details of the graphite crucible part in the AHP: (*1*) graphite baffle, (*2*) graphite container, (*3*) heating element, (*4*) graphite pedestal, (*5*) Monel pedestal rod, and (*6*) quartz tube

Heat was extracted axially from the growing crystal through a moving graphite pedestal (4), which is connected to a Monel pedestal rod (5). Cooling water circulated around this Monel pedestal rod. A quartz tube (6), placed inside the furnace, encased all of these parts of the AHP units.

Master alloy slugs (Al–4.5 wt% Cu) produced by Alcoa Inc., using a vacuum induction furnace were used for both AHP and DS experiments. In order to reduce oxidation of the metals during melting and freezing, the as-received slug was loaded in the apparatus, which was then evacuated to 10^{-1} torr with a mechanical pump and, subsequently, backfilled with argon. This evacuation/backfilling process was repeated several times. After purging the system, the argon atmosphere was substituted with the desired mixture of gas (Ar + H_2). The desired partial pressure of hydrogen in this gas mixture (P_{H_2} = 0–0.103 kg/cm^2) was achieved by controlling the ratio of Ar and H_2 flow. After melting, the melt was exposed to the gas mixture for 3 h, to allow the hydrogen concentration in the melt to reach being in equilibrium with the gas mixture. As shown in Fig. 2, the agreement between the hydrogen concentration in the processed samples measured by an Inert Gas Fusion (IGF) technique and those calculated by the Sievert's law indicates that the equilibration with the gas mixture had indeed taken place. It should be noted that the holding time would have allowed for entrapped oxides, if they were present in master alloy, to float on top of the melt. However, no noticeable oxide film was observed in any of the samples after the experiments.

Once the desired gas atmosphere was established, the baffle was positioned in the melt. The furnace temperature was slowly lowered so that the temperature at the location of thermocouple TC3 to reach at 645–650 °C. For both set of AHP and DS experiments, this location was designated to the beginning of the solidification. For the AHP experiments, the baffle temperature, measured at its center and edge in the baffle, was set at about 675 °C. This temperature setting allowed a constant distance of about 0.7–1 cm between the baffle and the dendrite tips, resulting in constant liquid thermal gradient of 19–25 °C/cm. For DS experiments, a thermocouple was immersed into the liquid before solidification to measure the thermal gradient, which was about 24 °C/cm. Following the establishment of the desired thermal gradients, the pedestal was translated down to the cold zone with various pre-set pulling speeds ranging from 0.00007 to 0.15 cm/s. It should be noted that a small clearance between the sides of the baffle and the crucible (about 0.5 mm) allowed liquid flow from above to below the baffle. This small gap was helpful in preventing the back diffusion of the solute into top melt as well as controlling the shape of the solidification front. The interface was generally flat or slightly convex. A convex shape of s/l interface was observed by switching the pulling rate from 0.00007 to 0.15 cm/s in the middle of the solidification process.

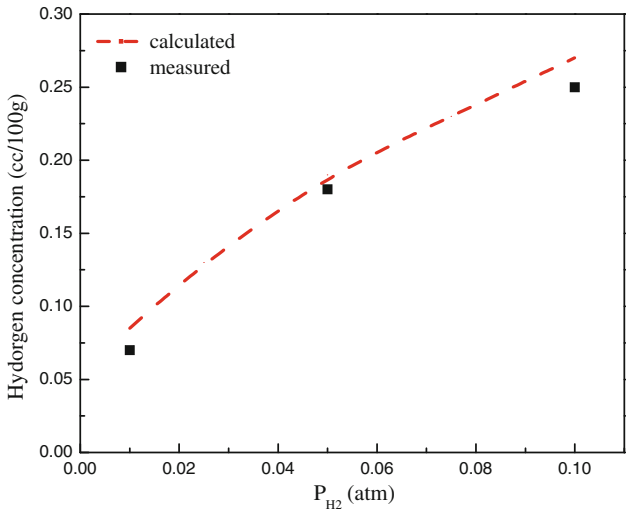

Fig. 2 Plot of hydrogen concentration measured by IGF sample and calculated by Sievert's law versus hydrogen partial pressure, P_{H_2}

After the solidification, the samples were sectioned in half along the longitudinal axes for metallographic analysis. Samples were grinded and polished up to 0.3 μm alumina particles solution, and, then, etched by Keller's reagent (2.5% nitric acid + 1.5% hydrochloric acid + 1.5% hydrofluoric acid) for 15 s. In order to avoid the influence of etching on the porosity measurements, the etching conditions were kept the same for all samples. It is well known that a light etching can underestimate the porosity because of smeared metal on the pore while over-etching can result in over-estimation of porosity because of increased edge around pore. At least ten photographs were taken at every 1 cm of height using 50× magnifications, and each photograph was analyzed with an image analyzer (Image Pro 4.5 version) to identify pores. In general, between 80 and 100 pictures were collected from one sample to reduce error caused by the 2D image. For chemical analysis, Electron Probe Micro Analysis (EPMA) was performed to measure copper concentration, and IGF was used to determine the hydrogen concentration.

Results

Three types of porosities were mostly observed in the samples as shown in Fig. 3. The first type consisted of interdendritic porosity which was mostly adjacent to eutectic regions as shown in Fig. 3a. These types of interdendritic porosities were found mostly at cooling rates ranging from 0.0015 to 0.018 °C/s. The porosity shape was difficult to define as it conformed to the local

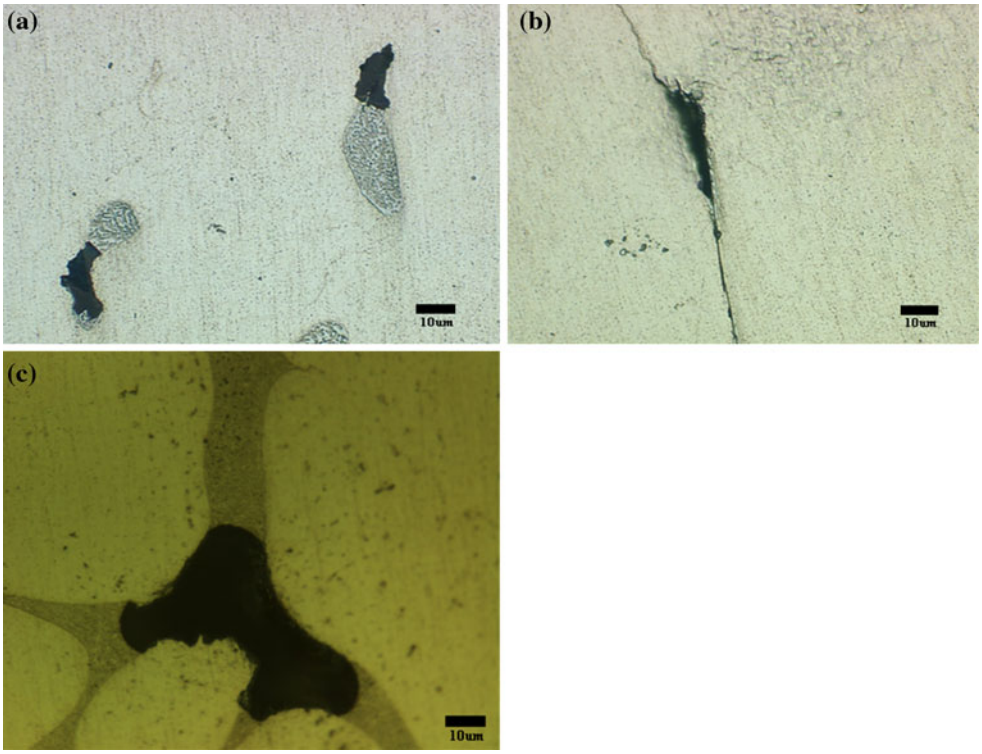

Fig. 3 Microporosity observation with optical microscope with ×500 magnification: **a** on the eutectic at cooling rate 0.012 °C/s, **b** on grain boundary of cell structure at cooling rate 0.018 °C/s, and **c** between dendrite colony (grain) at cooling rate 3.6 °C/s

microstructure. This is understandable, because the eutectic region corresponds to the final liquid just before the solidification is complete. Therefore, the pore size was usually smaller than the eutectic area size. Figure 3b shows the second type of porosity that was found at grain boundaries without containing an eutectic phase. This type of porosity is commonly called as secondary porosity because they form after the solidification from the super-saturated hydrogen in the solid. The secondary pores were very rare compared to the other types of pores, and their presence can be practically ignored for the current alloy in this study. Talbot and Granger [12] have pointed out that the secondary porosity is only pronounced in pure metals following a prolonged heat treatment at high temperature. For alloys and as-cast low purity metals, they can be ignored because they have larger interphase (eutectic) areas. Figure 3c shows another type of interdendritic porosity, which was observed at high cooling rate of 3.6 °C/s. This type of porosity tended to be located at the junction between dendrite colonies (grains), which had mostly equiaxed structure with fine dendrite arm spacing at this high cooling rate.

The average volume percentage porosity of DS and AHP samples versus the initial hydrogen concentration is plotted in Fig. 4. For both sets of experiments, the volume percentage of porosity increases with the initial hydrogen concentration. However, for the AHP samples, the average

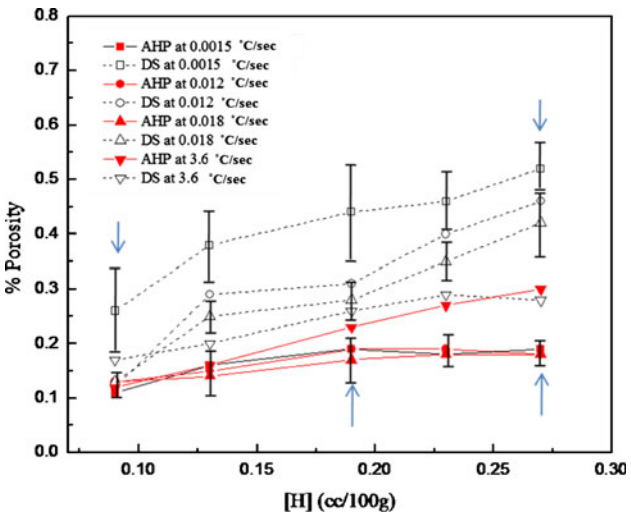

Fig. 4 Comparison of volume % porosity between AHP (*solid lines*) and DS (*dotted lines*) samples according to the change of initial hydrogen concentration at different level of cooling rates: 0.0015, 0.012, 0.018, and 3.6 °C/s

porosity level is considerably lower by 20–40% than that of the DS samples. The reduction in the volume percentage is particularly more at higher initial hydrogen concentrations and lower cooling rates. Moreover, the porosity level of AHP samples reaches a plateau, particularly, at lower cooling rates as the initial hydrogen concentrations

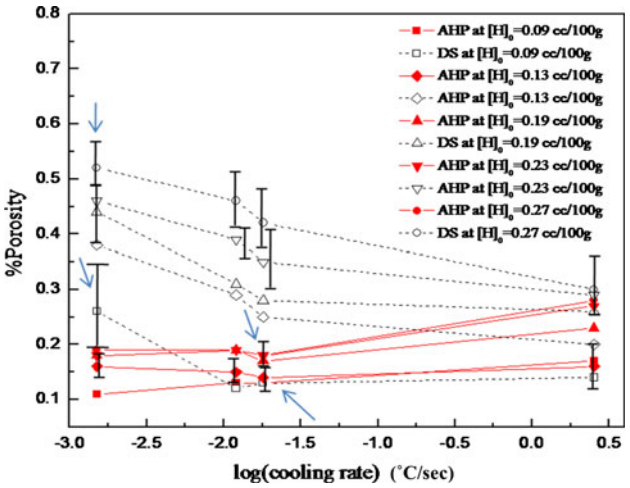

Fig. 5 Comparison of volume % porosity between AHP (*solid lines*) and DS (*dotted lines*) samples according to the change of cooling rate at different level of initial hydrogen concentration

increases. In addition, error bars with arrows in Figs. 4 and 5 were obtained through repeated experiments (five times at the same conditions) and error bars without arrows were obtained by measuring the same sample after peeling off the previously measured surface to ensure reproducibility of experiments. The influence of the cooling rate on the porosity for both the DS and AHP samples is shown in Fig. 5. For the DS samples, as previous investigations observed [14, 24], the volume percentage of porosity tends to decease as the cooling rate increases. On the other hand, the volume percentage of porosity of the AHP samples is not as sensitive to the cooling rate as the DS samples at 0.0015–0.018 °C/s. When the cooling rate exceeds 0.018 °C/s, the volume percentage of porosity in the AHP samples becomes as high as that in the DS samples, regardless of the initial hydrogen concentrations. Figures 4 and 5 show that the reduction of porosity is greater at the higher initial hydrogen concentration and slower cooling rate when the AHP technique is used.

Discussion

Porosity can form because of volume shrinkage during solidification and/or because of nucleation and growth of dissolved gases in the liquid. For both cases, pore growth will depend strongly on the balance between various pressure terms. For DS, these terms include the pressure drop (ΔP) between the dendrites, the gas pressure (P_g) inside a gas pore, the external pressures such as the atmospheric pressure (P_a), the pressure generated by surface tension (P_σ), and metallostatic head pressure (P_ρ) of the melt. The pressure balance between a pore and its surroundings is given by the following Eq. 1:

$$\Delta P + P_g = P_a + P_\sigma + P_\rho. \quad (1)$$

For a given pore size and location, if the sum of ΔP and P_g is greater than the external pressures on the right side of Eq. 1, the pore can grow until both sides are balanced. As discussed below, for a given casting geometry and alloy system, the pressure terms, and, consequently, the gas porosity will depend on the hydrogen content in the liquid, alloy composition, solidification rate, and temperature gradient in the liquid.

(1) Pressure drop (ΔP)

Piwonka and Flemings [25] suggested a fundamental model with which to calculate the pressure drop in interdendritic regions. Based on D'arcy's equation, this model assumes the dendritic structure as simple pipe structure. Recently, Sigworth and Wang [26] developed a more realistic model by changing from this simple pipe structure to the semi-spherical dendrite tip, where the pressure drop is not conspicuous. With these assumptions, the pressure drop is calculated as follows:

$$\Delta P = -\frac{\mu\beta}{(1-\beta)} 8\pi t^3 \frac{V\Delta T}{G_L d_l^2} \ln\frac{\alpha}{1-g_s}, \quad (2)$$

where α is the geometrical portion of interdendritic feeding, g_s is solid fraction in the mushy zone, $\beta(=(\rho_s-\rho_L)/\rho_L)$ is the contraction factor, G_L is the thermal gradient, V is the solidification rate, and t is the tortuosity of the dendrite.

(2) Gas pressure (P_g)

Since hydrogen is the only gaseous element with measurable solubility in the Al–Cu (4.5 wt%) alloy [11, 27, 28], Poirier et al. [29] calculated the hydrogen concentration in the Al–Cu melt with a simple mass balance of

$$[H] = [H]_0/[1-g_s(1-k_H)], \quad (3)$$

where $[H]$ is the concentration of hydrogen in the liquid, $[H]_0$ is the initial concentration of hydrogen in the liquid before solidification, $k_H(=181/T-1.369)$ is the distribution coefficient of hydrogen [29], and g_s is solid fraction in the mushy zone. Equation 3 can be transformed into the pressure term using Sievert's law:

$$P_{H_2} = \left(\frac{f_H[H]}{S}\right)^2, \quad (4)$$

where f_H is the activity coefficient and S is Sievert's constant ($cm^3\ atm^{1/2}/100\ g$). The gas pressure inside the pore can then be calculated by combining Eqs. 3 and 4:

$$P_{H_2} = \left(\frac{f_H[H]}{S}\right)^2 \left(\frac{1}{1-g_s(1-k_H)}\right)^2, \quad (5)$$

where $P_H^0 = (f_H \cdot [H]/S)^2$, which indicates the initial gas pressure before the solidification. Equation 5 conveniently

relates the change in the hydrogen gas pressure during solidification to the solid fraction, g_s, using k_H for Al–H liquid. However, it should be noted that the copper concentration also changes from 4.5 to 33 wt% inside the mushy zone, which can lead to a change in hydrogen solubility.

Opie and Grant [12] determined the solubility of hydrogen in Al–Cu alloys with copper concentrations up to 32 wt% and 600 °C < T < 1000 °C as follows:

$$\mathrm{Log}_{10}S = -\frac{A}{T} + B \tag{6}$$

$A = 2550 + 358.9C_{Cu}^{1/2} - 54.48C_{Cu} + 0.6241C_{Cu}^{1/2}$, $B = 2.620 + 0.3043C_{Cu}^{1/2} - 0.08072C_{Cu} + 0.004484C_{Cu}^{3/2}$, and S is the hydrogen solubility in 1 cm^3 of H_2 gas per 100 g of Al–Cu alloy, in equilibrium with 1 atm pressure of H_2. Using Eq. 6, one can estimate the change in solubility of hydrogen in Al–Cu (4.5 wt%) and the solubility change along the dendrite height.

(3) Pressure against surface tension (P_σ)

Considering the geometry of dendrites, Sigworth and Wang [26] expressed pressure against the surface tension of the pore as follows:

$$P_\sigma = 4\sigma/g_l d_l, \tag{7}$$

where σ is the surface tension (dyne/cm or g/s^2) between the liquid and the pore, g_l is the liquid fraction, and d_l is the dendrite arm spacing. The surface tension can be also affected by the alloying elements. For Al–Cu (4.5 wt%), Poirier and Sperser [30] estimated the pressure against the surface tension in the Al–Cu alloy system as:

$$\sigma = 868 + 0.721 \cdot C_{Cu} + 0.0129 \cdot C_{Cu}^2, \tag{8}$$

where C_{cu} is the concentration of copper (wt%). By inserting Eq. 8 into Eq. 7, the surface tension variation along the dendrite can be estimated.

In sum, by integrating Eqs. 2, 5, and 8 into Eq. 1, the overall external and internal pressures acting on a pore can be written as:

$$P_\rho + P_a + \frac{4\sigma}{g_l d_l} = \frac{\mu\beta}{(1-\beta)} 8\pi t^3 \frac{R\Delta T}{G d_l^2} \ln\frac{\alpha}{1-g_s} + P_H^0 \left(\frac{1}{1-g_s(1-k)}\right)^2. \tag{9}$$

where P_a is 1.03 kg/cm^2 (or 1 atm), P_ρ is the $\rho_L g h$, g is the gravitational acceleration constant, ρ_L is the liquid density, and h is the sample height.

Equation 10 indicates that, for a given casting geometry and alloy system, the gas porosity will depend on the initial hydrogen content in the liquid, alloy composition, solidification rate, and temperature gradient in the liquid. The calculated effects of the solid fraction on the gas pressure and other pressure terms in the DS samples are summarized in Fig. 6a for various initial hydrogen concentrations and cooling rates in this study. The pressure terms are calculated by Eqs. 2, 5, and 8 using parameters summarized in Table 1 at cooling rates of 0.0015, 0.012, 0.018, and 3.6 °C/s. From the above calculation, a critical solid fraction, g_s^*, above which the gas pressure inside the pore exceeds the sum of all other gas pressure terms, $P_a + P_\sigma + P_\rho - \Delta P$, can be found. This critical solid fraction as a function of the initial hydrogen content at different cooling rates is plotted in Fig. 6b. A small g_s^* indicates that gas bubbles can nucleate in the early stages of solidification near the dendrite tip. Increasing the cooling rate can push the critical solid fraction back slightly by

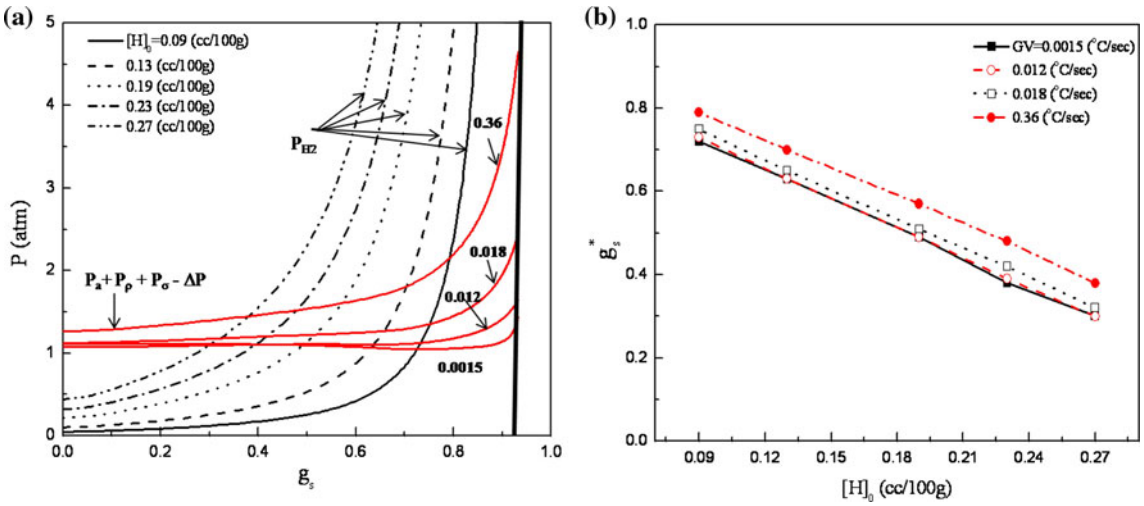

Fig. 6 **a** Comparison of the gas pressure term with other pressure terms according to the change of initial hydrogen contents ($[H]_0$ = 0.09, 0.13, 0.19, 0.23, and 0.27 cc/100 g) and cooling rates (cooling rate = 0.0015, 0.012, 0.018, and 0.36 °C/s) when samples are solidified with DS technique. **b** Corresponding critical solid fraction according to the initial hydrogen content

Table 1 Physical and thermochemical parameters for Al–Cu (4.5 wt%) alloy

Symbol	Parameter	Unit	Reference
ρ_L	Liquid density	2.42 g/cm^3	[43]
ρ_s	Solid density	2.59 g/cm^3	[43]
m_l	Liquidus slope in phase diagram of Al–Cu	3.3 °C/wt%	[43]
D_L	Diffusivity of copper in liquid aluminum	4.5×10^{-5} cm^2/s	[44]
D_S	Diffusivity of copper in solid aluminum	1.7×10^{-8} cm^2/s	[44]
$D_{H,L}$	Diffusivity of hydrogen in liquid aluminum	3.0×10^{-3} cm^2/s	[45]
$D_{H,S}$	Diffusivity of hydrogen in solid	5.2×10^{-4} cm^2/s	[45]
k_L	Thermal conductivity of liquid	90 J/s m K	[43]
k_S	Heat conductivity of solid	174 J/s m K	[43]
α_L	Thermal diffusivity of liquid	0.321 cm^2/s	[43]
α^*	Thermal expansion coefficient	0.000027/K	[43]
μ	Viscosity of liquid	0.045 g/cm s	[45]
C_l	Heat capacity of liquid	1.18 J/g k	[43]
C_S	Heat capacity of solid	0.9 J/g k	[43]
σ_0	Interfacial energy of aluminum	847 g/s^2 or dyne/cm	[30]
T_m	Liquidus temperature	648 °C	[43]
k_H	Hydrogen distribution coefficient	NA	[29]
t	Tortuosity	2	[25]

affecting P_σ. However, the initial hydrogen concentration has a much more pronounced influence on g_s^*, as shown in Fig. 6b. This finding is in line with the observations in Figs. 4 and 5. The threshold hydrogen concentration below which gas porosity can be avoided is obtained when the gas pressure, P_g, does not exceed $P_a + P_\sigma + P_\rho - \Delta P$ at the dendrite root. For example, at a cooling rate of 3.6 °C/s, the calculated pressure of $P_a + P_\sigma + P_\rho - \Delta P$ at the eutectic point is 4.73 atm. According to Eq. 5, it can be seen that the gas pressure cannot reach this level unless the initial hydrogen content is more than 0.03 cc/100 g.

Comparing AHP results with results of DS samples, it is observed that AHP is noticeably less sensitive to process variables. A key feature of the AHP technique is the placement of a baffle near the s/l interface, so the melt height, which is the distance from the s/l interface to the free surface, must to be re-defined as the distance between the s/l interface (or dendrite tip) and the baffle. This, in turn, influences the level of convection which is related to the melt height through the Rayleigh number, Ra_W for a bulk liquid as given below;

$$Ra_W = \frac{g\alpha^* \cdot 2(T_s - T_m)h^4/d}{\upsilon \cdot \alpha_L}, \quad (10)$$

where g is the magnitude of the acceleration due to gravity, α^* is the thermal expansion coefficient in liquid, d is the diameter of the sample, T_s is the temperature at the free surface, and T_m is the liquidus temperature. An increase of Ra_W value, representing the ratio of the buoyancy force to the viscous force, indicates more convective mixing in the liquid.

For a given alloy, convection is strongly influenced by the melt height, h. At the beginning of solidification, the melt height, h, of DS samples is almost equal to its sample height (=7–8 cm), but it decreases as the solidification proceeds. In contrast, for the AHP samples, the melt height, which is the distance between the bottom of the baffle and s/l interface (=dendrite tip), is about 0.7–1 cm and remains constant throughout the entire solidification process. As such, the Rayleigh number of AHP samples is lower by almost four orders of magnitude, meaning that the melt will be less convective below the baffle. The convection can affect solidification behavior, especially solute redistribution, so, by examining the composition of the dendrite tip, we can assess the degree of convection indirectly, as discussed below.

The copper concentration across dendrite arms was measured at 5 cm height for DS and AHP samples using EPMA, as shown in Fig. 7, in which the minimum concentration at the center of the dendrites for the AHP samples is generally higher than those of the DS samples, especially at slow cooling rates. By correcting for the back solid state diffusion [31], the core composition corresponds to 0.91 wt% for the DS sample and 1.50 wt% for the AHP sample at a cooling rate of 0.0015 °C/s at the moment. The corresponding tip temperatures are 643 °C for 0.91 wt% of copper composition and 633 °C for 1.50 wt%. By a similar procedure, the tip composition of DS and AHP were found to be 0.91 and 0.93 wt%, respectively, at a cooling rate of 0.018 °C/s. The results indicate that the tip composition difference between the AHP and the DS samples is discernable only at a slow cooling rate. Herein, because of

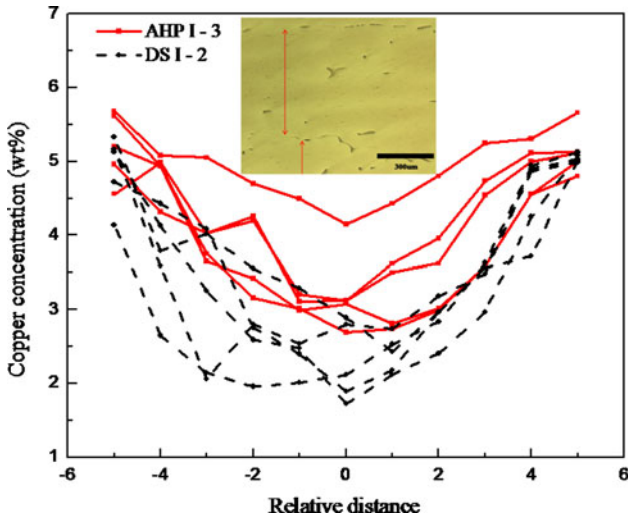

Fig. 7 Comparison of copper composition profile between AHP and DS samples within dendrite at cooling rate 0.0015 °C/s (the scanned region is marked in the photomicrograph with *arrow*)

higher tip composition of the AHP sample relative to the DS sample, the thickness of the mushy zone in the AHP samples is somewhat shorter than that for the DS samples.

In Fig. 8, the tip compositions measured at cooling rates of 0.0015 and 0.018 °C/s are compared to theoretical calculations using Burden and Hunt's model [32, 33] and Alexandrov's model [34]. The former assumes no convective mixing in the bulk liquid, whereas the latter assumes medium convection in the melt. Although the tip temperature of AHP sample at a slow cooling rate of 0.0015 °C/s is obviously closer to Burden and Hunt's model, it is still about 10 °C higher than that obtained by Burden and Hunt's model. This difference may be caused by the presence of weak convection in the AHP samples.

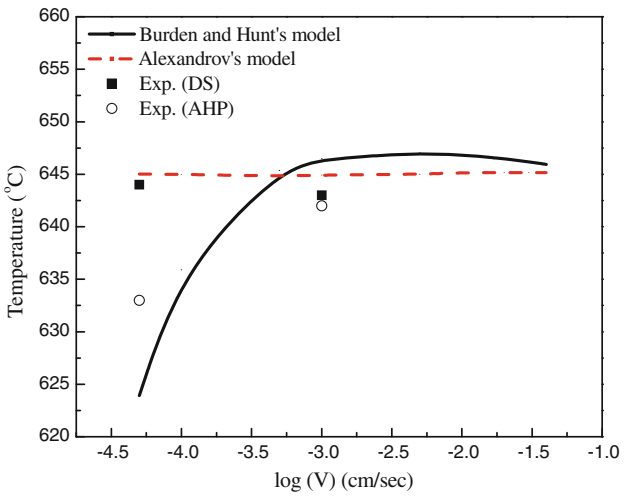

Fig. 8 Comparison between tip temperature measured by EPMA and calculated by Burden and Hunt's model (*solid line*) and Alexandrov's model (*dotted line*)

However, we can still conclude that AHP technique suppresses convection considerably, resulting indifferent copper concentrations and the thickness of the mushy zone.

Another important influence of the AHP technique is present due to the "zone" effect, by confining the liquid between the dendrite tip and the baffle. In Fig. 9, the conceptual phenomenon ahead of the dendrite tip is depicted to explain the zone effect. When the diffusion boundary layer ahead of the dendrite tip exceeds beyond the baffle, the rejected solutes from the s/l interface fails to dissipate into the bulk liquid and can build up in this confined zone. For a planar s/l interface, the thickness of the diffusion boundary layer can be roughly estimated by $2D/V$ [35, 36], where D is the diffusivity of the solute and V is the solidification rate. For copper solute, the calculated thicknesses of the diffusion boundary layer are 0.65, 0.18, 0.11, and 0.006 cm for cooling rates of 0.0015, 0.018, 0.012, and 3.6 °C/s, respectively. For hydrogen, the calculated thicknesses are 84, 12, 7.5, and 0.4 cm for the same cooling rates, respectively. In this regard, solute accumulation for copper is expected to be less pronounced because its diffusion boundary layer is much thinner than the melt height of AHP samples (=0.7–1.0 cm) for the planar s/l interface. It should be noted that, for the dendritic solidification, the diffusion boundary layer thickness must be shorter than $2D/V$ because the dendrite tip is more efficient in dissipating solutes [36]. If we assume the dendrite tip as a hemisphere shape, the diffusion boundary layer is approximately equal to the tip radius, R, and the approximate tip radius can be calculated using Eq. 11 as follows [36]:

$$R = \frac{2D_{\mathrm{Cu}}}{V} + \frac{2mC^{0}_{\mathrm{Cu}}}{G_l} \tag{11}$$

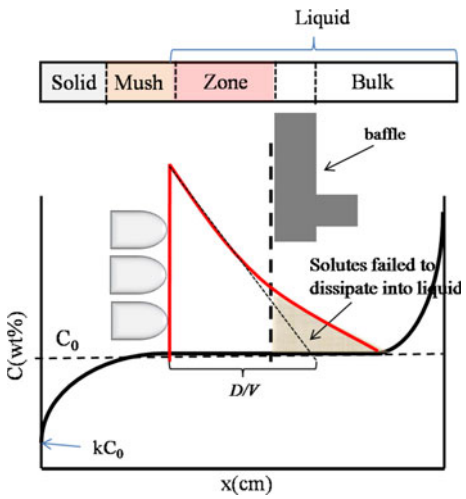

Fig. 9 Mechanism of hydrogen buildup below the baffle

where V is the solidification rate, D_{Cu} is the diffusion coefficient of copper, C^*_{Cu} is the initial copper concentration, G_l is the temperature gradient, and m is the tangent of the liquidus line in the Al–Cu phase diagram. The calculated results are 2.7, 1.4, 1.3, and 0.11 cm for cooling rates of 0.0015, 0.012, 0.018, and 3.6 °C/s, respectively. Based on these calculations, the presence of the baffle influences hydrogen buildup only at the low cooling rates. At high cooling rate of 3.6 °C/s, it will be negligible because of the thinner diffusion boundary layer than the melt height in AHP samples. It is likely that this resulted in the observed similarity of the porosity amount between the DS and the AHP samples at a high cooling rate, as shown in Figs. 4 and 5.

To verify the hydrogen buildup below the baffle, a special experiment was designed by inserting four pins at 4 cm height on a container. The baffle would stick to those pins after partial solidification and remained stationary afterward. In continuing solidification, the baffle was engulfed by the growing solid, and the remaining melt solidified above the baffle the same as that in the DS experiments. The as-solidified sample was then sectioned normal to the growth direction, and hydrogen concentration was determined using the IGF technique. The results are plotted in Fig. 10, which shows a noticeable increase in the hydrogen concentration just below the baffle, where the hydrogen concentration reached 0.21 cc/100 g. Above the baffle, the hydrogen concentration is about 0.07–0.08 cc/100 g, which is close to calculated hydrogen concentration

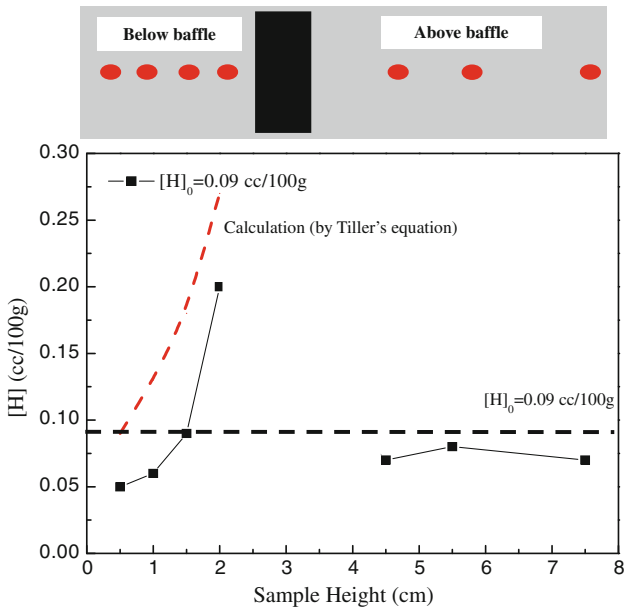

Fig. 10 Hydrogen concentration below and above the baffle according to sample height at cooling rate 0.018 °C/s and $[H]_0 = 0.09$ cc/100 g. Measurement points and baffle location is described schematically on *top*

of 0.09 cc/100 g by Sievert's law. To have porosity, the hydrogen bubbles should be trapped between dendrites. If the hydrogen bubbles are nucleated near the dendrite tip, they have a better chance to escape to free surface. Therefore, nucleation location of the hydrogen bubbles on the dendrites is important.

Recently, using an in situ X-ray temperature gradient stage (XTGS) technique [37] showed that almost 95% of the gas bubbles are nucleated when the hydrogen concentration exceeded its solubility limit by 1.1–3.1 times (see Fig. 3 in [37]). In addition, once numerous gas bubbles nucleate in a certain range, a considerable amount of hydrogen was consumed, and rejected hydrogen atoms in the continuing solidification were incorporated into these newly formed bubbles. Thus, most of the pores were present in this specific supersaturation range along the mushy zone, and the number of pores decreased toward the bottom of the mushy zone [38]. Han and Viswanathan [39] also claimed that the nucleation and the subsequent growth of pores could consume hydrogen and reduce the hydrogen concentration around the bubbles, which halted bubble nucleation. They also proposed that subsequent nucleation does not resume until enough hydrogen is built up again after the continuing solidification. This hypothesis was supported by a water solidification experiment conducted by Carte [40] in which, gas (air) bubbles were nucleated on the dendrite, but no other bubbles were nucleated during its growth.

With supersaturation ratio of 1.1–1.3, the nucleation zone inside the dendrite can be calculated by multiplying the supersaturation ratio by the original solubility, S, in Eq. 5. The newly calculated gas pressure that accounts for the supersaturation effect, can be obtained with the aid of Eq. 9. In the case of the AHP samples, initial hydrogen concentration is not constant as it is in the DS samples, because hydrogen keeps accumulating during solidification until it reaches a steady state. The amount of excess solute buildup (see the gray area in Fig. 9) below the baffle can be calculated using a modified Tiller's equation [41] in which the term D/V for planar front solidification is replaced by $2/R$ for cellular solidification as follows

$$C = C_0 \frac{1 - k_H}{k_H} \frac{R}{2} \exp\left(-\frac{2x'}{R}\right), \tag{12}$$

where k_H is the equilibrium partitioning constant of hydrogen, x' is the distance from the dendrite tip to the baffle, and R is the curvature of the dendrite tip obtained from Eq. 11. The excess hydrogen built up under the baffle can then be calculated numerically using Eq. 12. For example, the calculated hydrogen concentration at 4 cm height is 1.1 cc/100 g at $[H]_0 = 0.09$ cc/100 g. By using this hydrogen concentration ($[H] = 1.1$ cc/100 g) as the initial hydrogen concentration to calculate Eqs. 3–5 for the

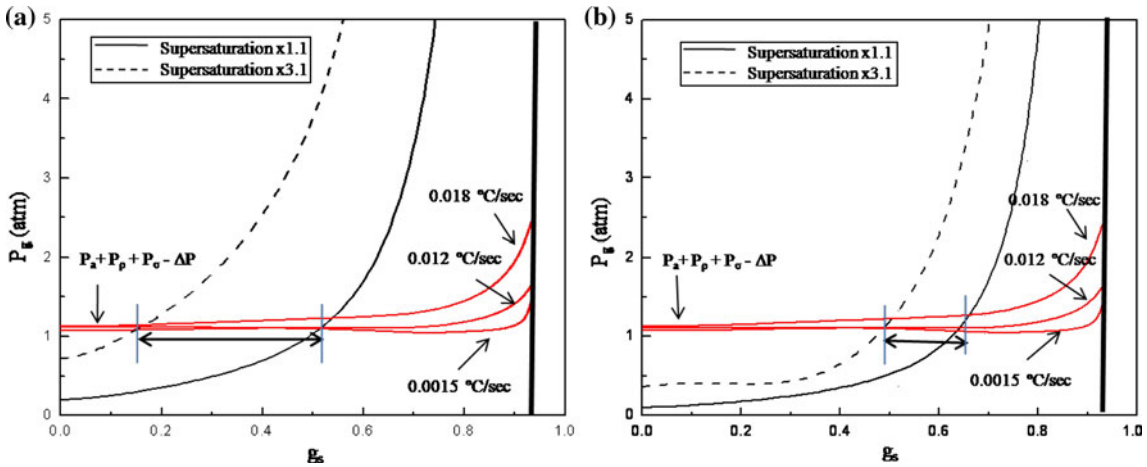

Fig. 11 Calculated nucleation ranges versus the cooling rate: **a** AHP sample at $[H]_0 = 0.09$ cc/100 g and **b** DS samples for $[H]_0 = 0.27$ cc/100 g: *dotted line* represents the supersaturation ratio of 1.1 and *solid line* is 3.1

AHP samples, we can insert this value into Eq. 9 to obtain pore nucleation range.

Figure 11a and b show the nucleation ranges when $[H]_0$ is 0.09 and 0.27 cc/100 g for the AHP and DS samples, respectively. In this figure, the calculated gas pressures including the supersaturation effect are plotted as a function of the cooling rate; the dotted line is the case when supersaturation is 1.1 and the solid line is for 3.1. These pressures are directly compared with $P_a + P_\rho + P_\sigma - \Delta P$ according to the cooling rate of 0.0015, 0.012, and 0.018 °C/s, respectively. The nucleation ranges, denoted by the arrow in the figure, are found between two intersection points of the newly calculated P_g and the $P_a + P_\rho + P_\sigma - \Delta P$. Comparing with Fig. 6a, the starting point of possible nucleation in the DS samples retreats from $g_s = 0.32$–0.44. For the AHP samples, $[H]_0 = 0.09$ cc/100 g is selected as a representative example to show the nucleation range. The hydrogen bubble nucleation range for the AHP samples is approximately in $g_s = 0.14$–0.51, regardless of cooling rates. This indicates that the gas bubble nucleation in the AHP samples occurs closer to the dendrite tip than in the DS samples. The location of the hydrogen bubble nucleation is important, since the gas bubbles nucleated at or near the dendrite tip have a much better chance to escape from the dendrites to the free surface. In the AHP technique, however, the hydrogen bubbles may not escape all the way to the free surface, since the baffle interfere them and these escaping gas bubbles will be stuck under the baffle by consuming continuously rejected hydrogen during the solidification. This was verified by another set of AHP experiment with Ni–Mo–Ta–Al alloy [42]. The results from a quenched sample showed the dispersion of large pores that is about 100–200 μm in diameter, below the baffle, as compared with normal pores which are typically 7–15 μm. The large pores form by the agglomeration of the gas bubbles escaping the dendritic region.

In summary, it is believed that hydrogen bubbles in the AHP samples nucleate near the dendrite tip and escape without being trapped in the mushy zone. The gas bubbles are stationary, because of the baffle. These gas bubbles consume rejected hydrogen atoms during solidification, and restrict the nucleation of the new gas bubbles. At the end of solidification, the baffle will leave from the liquid melt and, eventually, the large hydrogen bubbles can escape to the free surface. Concomitant with the above is the reduction in the thickness of the mushy zone in the AHP samples because of the suppressed convection. The reduction in the mushy zone thickness also favors escape of gas bubbles.

It would be interesting if the AHP solidification technique can be applied to well-developed alloy systems such as Al–Si–Mg or peritectic system such as Fe–Ni alloy.

Conclusions

The influence of the solidification process variables on porosity formation mechanism in Al–4.5% Cu alloy is investigated using AHP and normal DS technique. Samples produced by AHP contain microporosity about 20–40% less than that of samples prepared by DS. The reduction of the microporosity is more pronounced with decreasing the cooling rate and increasing the initial hydrogen concentration. These observations are explained by the influence of the AHP baffle on the suppression of liquid convection below the baffle by about three orders of magnitude and the enhanced hydrogen accumulation in the confined zone. It is

believed that both factors contribute to the nucleation of the gas bubbles closer to the dendrite tip in the AHP samples than in the DS samples, which enables their subsequent escape from the mushy zone.

Acknowledgements The authors would like to thank Dr. Men Chu Glen of Alcoa Research Center for providing the master alloys and for helpful discussion about this research.

References

1. Atwood RC, Spidhar S, Zhang W, Lee PD (2000) Acta Mater 48:405
2. Surappa MK, Blank E, Jaquet JC (1986) Scr Met 20:1281
3. Caceres CH (1995) Scr Met 19:224
4. Sonsino CM, Ziese J (1993) Int J Fatigue 15:75
5. Caceres CH, Selling BI (1996) Mater Sci Eng A220:195
6. Samuel AM, Samuel FH (1995) Mater Sci Eng 26A:2359
7. Flemings MC (1974) Solidification processing. McGraw-Hill, New York, p 148
8. Kattamis TZ, Coughlin J, Flemings MC (1967) Trans Met Soc AIME 239:1504
9. Walther WD, Adams CM, Taylor HF (1956) AFS Trans 56:658
10. Huang H, Suri VK, El-Kaddah N, Berry JT (1993) Modeling of casting welding and advanced solidification processes VI. TMS, Warrendale, p 219
11. Talbot DE (1975) Inter Metall Rev 20:166
12. Opie WR, Grant NJ (1950) Trans AIME J Met 188:1237
13. Chalmers B (1964) Principles of solidification. Robert E Krieger Publishing co. Inc., New York, p 289
14. Fang QT, Granger DA (1989) Light metals. TMS, Warrendale, p 927
15. Atwood RC, Lee PD (2000) Modeling of casting, welding, and advanced solidification processes, vol 4, p 599
16. Lee PD, See D, Atwood RC (1999) Proceedings in cutting edge of computer simulation of solidification and casting. Iron and Steel Institute of Japan, Osaka, Japan, p 97
17. Markworth AJ (1993) J Mater Sci Lett 12:1487
18. Li KD, Chang E (2004) Acta Mater 52:219
19. Golshev VD, Gonik MA (1996) Russian Patent, Application #4810464 (Feb 1990), Publication #1800854 (June 1996)
20. Balikci E, Deal A, Abbaschian R (2004) J Cryst Growth 262:581
21. Ostrogorsky AG, Mosel F, Schmidt MT (1991) J Cryst Growth 110:950
22. Ostrogorsky AG, Sell HJ, Scharl S, Müller G (1993) J Cryst Growth 128:201
23. Ostrogorsky AG, Müller G (1994) J Cryst Growth 137:66
24. Golyshev VD, Gonik MA, Tsetovskii VB (1999) J Cryst Growth 198/199:501
25. Piwonka TS, Flemings MC (1966) Trans Metall Soc AIME 236:1157
26. Sigworth GK, Wang C (1993) Metall Trans B 24B:349
27. Eichenaeur W (1968) IBID 59:613
28. Ransley CE, Neufeld H (1948) J Inst Metals 74:599
29. Poirier DR, Yeum K, Maples AL (1987) Metall Trans A 18A:1979
30. Poirier DR, Speiser R (1987) Metall Trans A 18A:1150
31. Bower TF, Brody HD, Flemings MC (1966) Trans AIME 236: 624
32. Burden MH, Hunt JD (1974) J Cryst Growth 22:99
33. Burden MH, Hunt JD (1974) J Cryst Growth 22:109
34. Alexandrov DV (2001) Acta Mater 49:759
35. Zener C (1949) J Appl Phys 20:950
36. Kurz W, Fisher DJ (1985) Fundamentals of solidification, 2nd edn. Trans Tech Publications Ltd., Netherlands, p 21
37. Lee PD, Hunt JD (1997) Scr Mater 36:399
38. Chai G, Backerrud L, Arnberg T, Metallk Z (1995) 86: 54
39. Han Q, Viswanathan S (2002) Metall Mater Trans A 33A:2067
40. Carte AE (1961) Proc Phys Soc 77:757
41. Tiller WA, Jackson KA, Rutter JF, Chalmers B (1953) Acta Met 1:1
42. Kim J, Abbaschian R (2009) Influence of solidification variables on microporosity formation of Al–Cu (4.5 wt%) alloy with axial heat processing. Dissertation, University of Florida, 2008, Gainesville
43. ASM Handbook Committee (1986) Metal handbook, vol 3. ASM International, Materials Park
44. Sareal JA, Abbaschian GJ (1986) Metall Trans A 17A:2063
45. Poirier DR (1987) Metall Trans B 18D:245